Supplementary Information

Stabilizing Perovskite Solar Cells at 85 °C *via* Additive Engineering and MXene Interlayers

Fanny Baumann[1], Jessica Padilla-Pantoja[1], Jose Manuel Caicedo-Roque[1], Masoud Karimipour[1], Naji Vahedigharehchopogh[1], Jose Santiso[1], Belén Ballesteros[1], Ramses A. Miranda Gamboa[1], Zhenchuan Tian[1], Sonia R. Raga[1]*, Monica Lira-Cantú[1]*.

1. Catalan Institute of Nanoscience and Nanotechnology (ICN2), CSIC and the Barcelona Institute of Science and Technology (BIST), Building ICN2, Campus UAB, E-08193 Bellaterra, Barcelona, Spain.

Corresponding author emails: sonia.ruiz@icn2.cat, monica.lira@icn2.cat

Experimental Methods

Materials and PSC fabrication

Fabrication and material use was performed identical as in previous works by the group, with the difference of the halide perovskite (HP) composition variation to $Cs_{0.08}MA_{0.12}FA_{0.8}Pb(I_{0.88}Br_{0.12})_3$ and halide perovskite bulk additive modification with H3PP in accordance to previous work.[1, 2]

Materials. N, N-dimethylformamide (DMF, anhydrous, 99.8%), dimethyl sulfoxide (DMSO, anhydrous, 99.8%), chlorobenzene (anhydrous, 99.8%), acetonitrile (anhydrous, 99.8%), isopropanol (99.97%, anhydrous), and 4-tert-butylpyridine (TBP, 96%) were received from Merck Co. lead(II) bromide ($PbBr_2$, 99.99%), lead (II) iodide (PbI_2, 99.99%), formamidinium iodide (FAI), rubidium iodide (RbI, 99.99%), methylammonium iodide (MAI), and cesium iodide (CsI, 99.99%) were purchased from TCI chemicals. 2,2',7,7'-tetrakis(N,N'-di-p-methoxyphenylamine)-9,9'-spirobifluorene (Spiro-OMeTAD, spiro) was purchased from Xi'an Polymer Light Technology Corp. All chemicals are used as received without any further purification. Ti_3C_2 MXene powder was purchased from Nanochemazone, Canada. 3-phosphonopropionic acid (H3PP), tetrapropylammonium hydroxide (TPAOH, 58%), tetrabutylammonium hydroxide (TBAOH, 45%), tetramethylammonium hydroxide (TMAOH, 25%) were purchased from Sigma-Aldrich. Laser-patterned fluorine-doped tin oxide (FTO) 15 ohm·sq on 2.3 mm-thick soda lime glass (SLG) was purchased from Yingkou Shangneng Optoelectronic Material Co., Ltd.

Stacking. Devices were prepared in n-i-p stacking with structure FTO(0.5 µm) /TiO_2-c(80 nm)/TiO_2-mp(150 nm)/perovskite(400-450 nm)/spiro(200 nm)/Au (70 nm). (For device cross-section see Figure 1a, Figure 6a and Figure S9)

Procedures. FTO (16 Ω/sq.) substrates (2.5 cm × 1.5 cm) were etched using Zinc powder and HCl 4 M, brushed with 10% Hellmanex™ and then placed in a sonicating bath with sequential cleaning using 2% Hellmanex™ solution, Acetone, Isopropanol, for 30 min, 10 min, 15 min, respectively, followed by UV/Ozone cleaner for 20 min. Solution of 9 mL ethanol (96%), 0.4 mL of acetyl acetone, and 0.6 mL of Titanuim di-isopropoxide bis-acetyl acetonate, was deposited through O_2 spray-pyrolysis on 450 °C preheated substrates to obtain a 20 nm thick TiO_2 blocking compact layer. The mesoporous TiO_2 layer (TiO_2-mp) was deposited from solution of 1 mg TiO_2 paste (nanoparticles 30 nm) diluted in 6 g of ethanol, deposited by spin-coated at 5000 rpm for 20 s, dried at 85 °C and thereafter annealed at 450 °C for 30 min and cooled down naturally. Before being moved to a controlled N_2 atmosphere, samples were exposed to UV-Ozone for 25 min and transferred immediately to the glove box, maintained at 18-20 °C (H_2O: 1-1.5 ppm, O_2:3-6 ppm), for perovskite, interface modification and HTL layer deposition. 0.050 mL perovskite solution was spread over the substrates and span at 2000 rpm for 10 s and 6000 rpm for 30 s, and after

15 s of the second step, 0.2 mL of CB was injected instantly to the center of the substrate and after spinning, the film was quickly annealed at 100 °C for 20 min. HTL layer was deposited by drop casting 35 µL of Spiro solution spinning at 3800 rpm for 20 s. The 70 nm gold contact was deposited using a high vacuum PVD system with pressure below 8×10^{-7} atm.

Perovskite Solution. 548.6 mg of PbI_2 and 57.06 mg of $PbBr_2$ was dissolved in 1 mL of DMF:DMSO (4:1 volume ratio) and heated at 150 °C for 5 min and cooled down. Following, 27.02 mg of CsI, 178.94 mg of FAI, and 17.41 mg of MABr were measured in a separate vial and subsequently dissolved into the previous solution to form the perovskite $Cs_{0.08}MA_{0.12}FA_{0.8}Pb(I_{0.88}Br_{0.12})_3$ precursor solution. The solution was heated at 75 °C for 15 minutes.

Bulk functionalization. 4.5 µl of a H3PP in DMF (40 mg/ml) stock solution was injected into 0.5 ml of the prepared 3–cation perovskite solution and shaken 20 s before deposition as above.

MXene Ti_3C_2-T_x Delamination and H3PP functionalization. The MXene nanosheets were delaminated by mixing with 5 mL of TPAOH and stirring at room temperature (without sonication) under neutral gas atmosphere for 24 h, followed by washing with isopropanol and centrifugation and mixing with 5 mL of TBAOH. This process was repeated three times and the obtained solid was finally re-dispersed in 3 mL of isopropanol. 0.5 mg amount of 3-phosphonopropionic acid (H3PP) was dissolved directly in the 2 mL of green solution of delaminated MXene nanosheets and bath sonicated for 20 min. The solution was drop casted on top of the perovskite film and the film was annealed at 70 °C for 3-5 min, cooled down, followed by HTL (spiro) deposition.

Characterization methods

Following characterization methods were employed to acquire the information presented in this work.

Current Density Voltage measurements. J-V scans presented were performed in 4 different setups; Solar Simulator, white LED in PAIOS (Fluxim), Wavelabs LS-2 LED AAA solar simulator in LITOS (Fluxim) and white LED in XRD holder. Main measurements presented were performed in a class AAA solar simulator (HelioSim-CL60) measured under a halogen light source with AM1.5G filter calibrated with a Si reference cell to 1 sun (100 $mWcm^{-2}$) using a light aperture mask with an active area of 0.16 cm^2. Scans forward from -0.1 to 1.2 V and reverse from 1.2 to -0.1 V were performed at scan speed 100 mV/s with 20 mV steps using a Keithley Source Meter. In PAIOS, the white LED light intensity was adjusted to provide similar photocurrent on the PSC than under 1sun in the calibrated solar simulator, the light power measured with a spectrophotometer was ~1035 W^{-2}.

Operational Testing (LITOS-L3). PSCs were subjected to harsh, yet controlled, operational stressing at 85 °C and ~100 $mWcm^{-2}$ LED approximate AM1.5G illumination in nitrogen (N_2) atmosphere simultaneously as monitoring devices output at maximum power point tracking (MPPT), defined ISOS-L3.

Electrochemical Impedance Spectroscopy (EIS). EIS procedures were made with commercial equipment PAIOS 4.4.1 from Fluxim AG™. Impedance amplitude of 20.0 mV at one sweep of frequency from 4 MHz to 0.08 Hz in 40 steps with a logarithmic transition was recollected at the output to record the modulation of the electronic signal. The offset voltage was adjusted to V_{OC} during a light intensity array of [0.0001(3), 0.000373(4), 0.00139(5), 0.00518(6), 0.0193(7), 0.0720(8), 0.268(9), 0.83, 1(10)] x ~105 $mWcm^{-2}$ (Figure S2b) given by a cold white Cree® XLamp® XP-G LED (Figure S1b).

Photoluminescence (PL). Photoluminescence of the devices was measured with excitation using a 453.6 nm wavelength pulsed laser of area ~1 mm^2, shone from the back-side of the device at an angle of 50°, from the same incident-direction as sunlight during operation. Samples were kept at N_2 flow during measurements. Detection was performed by a TimeHarp 260 detector (s-t-n ratio > 32000:1) at the magic angle (54.7°) as mounted in the commercial PicoQuant FluoTime 300 equipment. The samples were measured in a sequence of PL, TRPL, PL, to observe how much the samples were affected by the prolonged (0-5 min) exposure of the laser during acquisition of the TRPL response.

X-ray diffraction (XRD). X-ray diffraction measurements were performed in a parallel beam optics configuration (Parabolic Mirror + D.S. Slit ¼°+ 2 mm mask), using a four-circle geometry Diffractometer Malvern-Panalytical X'pert Pro MRD. The setup uses a ceramic X-ray tube with Cu Kα anode (λ = 1.5418 Å) as source. The source path includes a horizontal ω-2θ goniometer (320 mm radius) and a Parabolic Mirror. On the detection side, a fast X-ray PIXcel area detector is used, which is a detector based on Medipix2 technology with a 256 x 256 pixels array.

Scanning Electron Microscopy (SEM). SEM images were obtained with a FEI Quanta 650F ESEM microscope at 15 kV acceleration voltages.

Transmission Electron Microscopy (TEM). High resolution transmission electron microscopy (HRTEM) images, high angle annular dark field scanning transmission electron microscopy (HAADF STEM) images and energy dispersive X-ray (EDX) spectra were acquired using an FEI Tecnai G2 F20 HR(S)TEM operated at 200 kV and coupled to an EDAX super ultra-thin window (SUTW) X-ray detection system. Samples were gently scratched from the device and the powder in dry form was deposited on top of a TEM holey carbon Cu grid.

S1. Light intensities and EIS analysis.

Figure S1A shows the light spectra with power intensities from the equipment used during experiments. Figure S1b shows spectra for the logarithmic array of light intensities from 0.001 to 103.5 $mWcm^{-2}$ employed during EIS studies, and the equivalent circuit with an additional RC current contribution for slow ionic related processes used to fit impedance measurements on PSCs (Matryoshka circuit, Figure S1c). [3, 4]

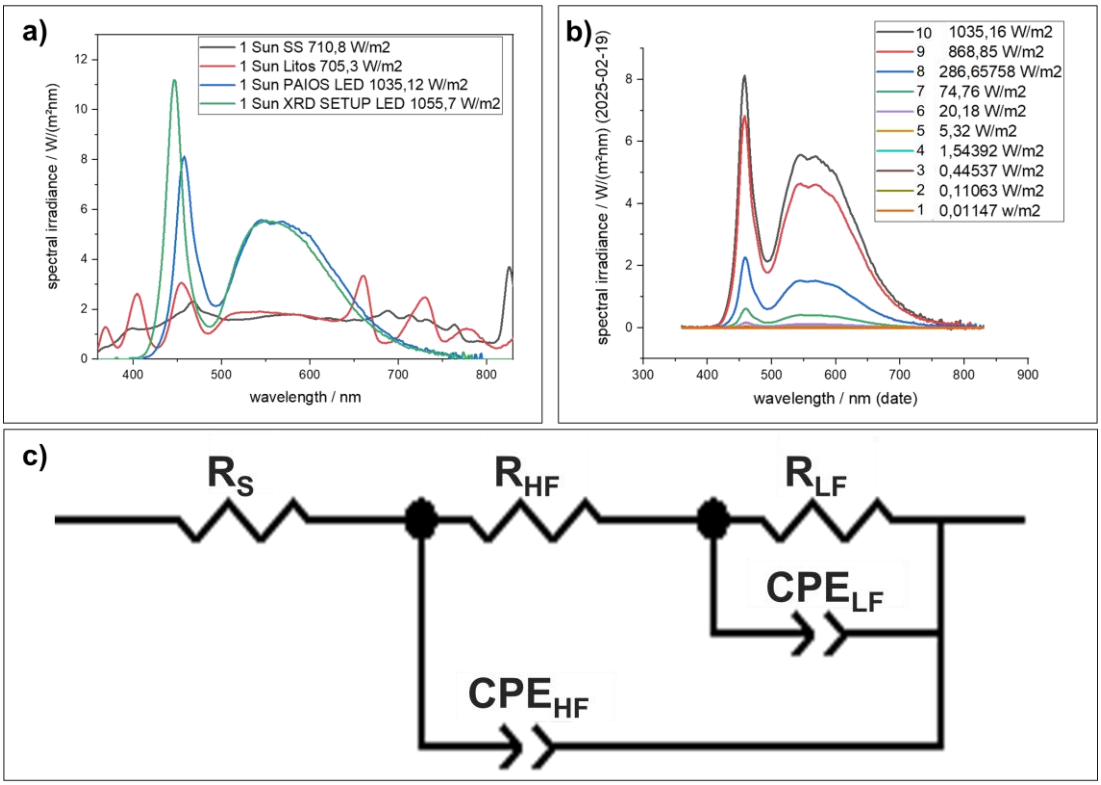

*Figure S1. a) illumination spectra between 350-820 nm for all light sources used during experiments b) light spectra in FLUXIM PAIOS at a variety of light intensities [0.0001, 0.000373, 0.00139, 0.00518, 0.0193, 0.0720, 0.268, 0.83, 1] *1000Wm^{-2}, and c) Equivalent circuit for EIS fittings.*

The time parameters for each of the frequency ranges where calculated from the parameters extracted from EIS fittings from the equivalent circuit in Figure S1c according to

$\tau_{LF} = R_{LF} \cdot C_{LF}$ and $\tau_{HF} = R_{HF} \cdot C_g \cdot 10^6$, from $C_g = \frac{(R_{HF} \cdot CPE_{HF})^{\frac{1}{n_{HF}}}}{R_{HF}}$ and $C_{LF} = \frac{(R_{LF} \cdot CPE_{LF})^{\frac{1}{n_{LF}}}}{R_{LF}}$. (Eq. S1)

where $\tau_{LF/HF}$, $R_{LF/HF}$, CPE and $C_{LF/HF}$ is the low-frequency(LF)/high-frequency(HF) time constant, resistance, constant-phase-element, and capacitance. C_g is the geometric capacitance, and n is the ideality factor.

Changes in the recombination mechanisms in the perovskite film are deduced by reduced slope of R_{SUM} vs. V_{OC} at the highest light intensities as

$$R_{rec} = R_0 \, exp\left(-\frac{qV}{n_{ap} k_B T}\right) \quad \text{(Eq. S2)}$$

where n_{ap} is the apparent ideality factor, q is the elementary charge, k_B Boltzmann constant and T the temperature. R_0 is the resistance at zero potential, dependent on the recombination rate constant (J_{rec0}) material band-gap (E_g) and indirectly by the built-in bias (V_{bi}).[5] Calculated n_{ap} values of the fresh REF and MOD devices in Figure 3b were 1.8 and 1.6, respectively while, after the stress, these values increased to a range of 2.6-2.7 for REF and 1.8-1.9 for MOD. The increased n_{ap} and reduced R_0 suggests that the stress test leads to higher recombination rates due to increased number of defect trap states, resulting in lowered V_{OC} at high light intensities.

S2. Reversibility phenomena after operational testing

Figure S2 presents parallel tendencies in reversibility of phenomena overserved on dark IV and the low light intensity feature τ_{LF}, was observed depending on how long time has passed after the operational test when EIS was measured.

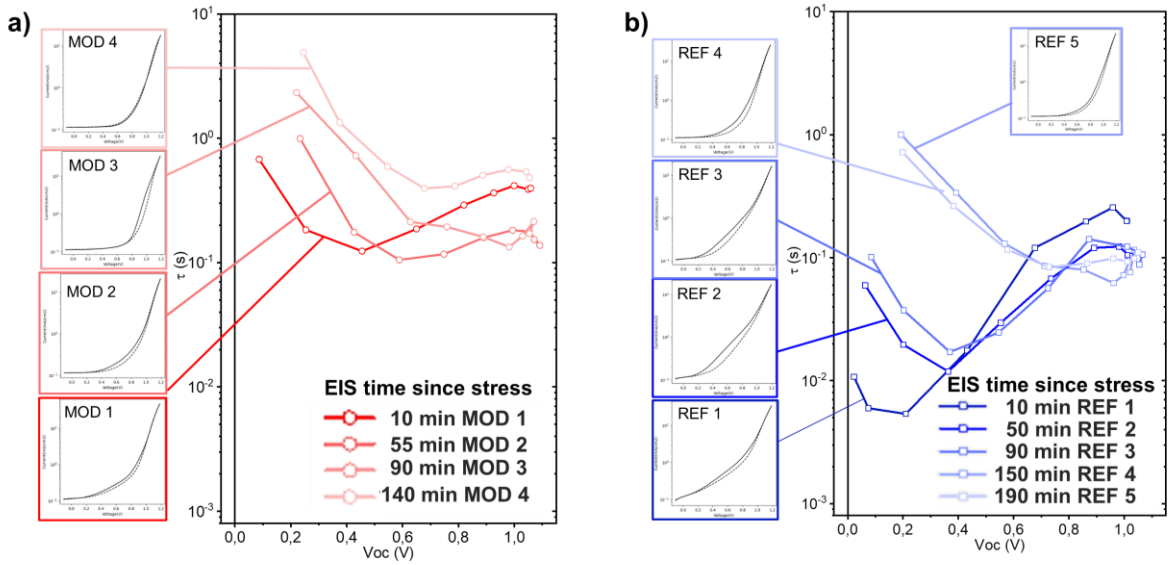

Figure S2. Low frequency time constant of EIS fittings (τ_{LF}) and dark IV curve depending on the time after operational stress test at 85 °C and 1 sun illumination at MPPT. a) MOD solar cell with H3PP:HP and MXene:H3PP modification b) reference (REF) solar cell.

S3. Feature changes on EIS experimental data

After operation at ~100 mWcm^{-2} and 85 °C, both the REF and the MOD low frequency signal contribution shifted right and increased, however for MOD devices the increase in ion-related contributions was delayed, as visualized by Figure S3.

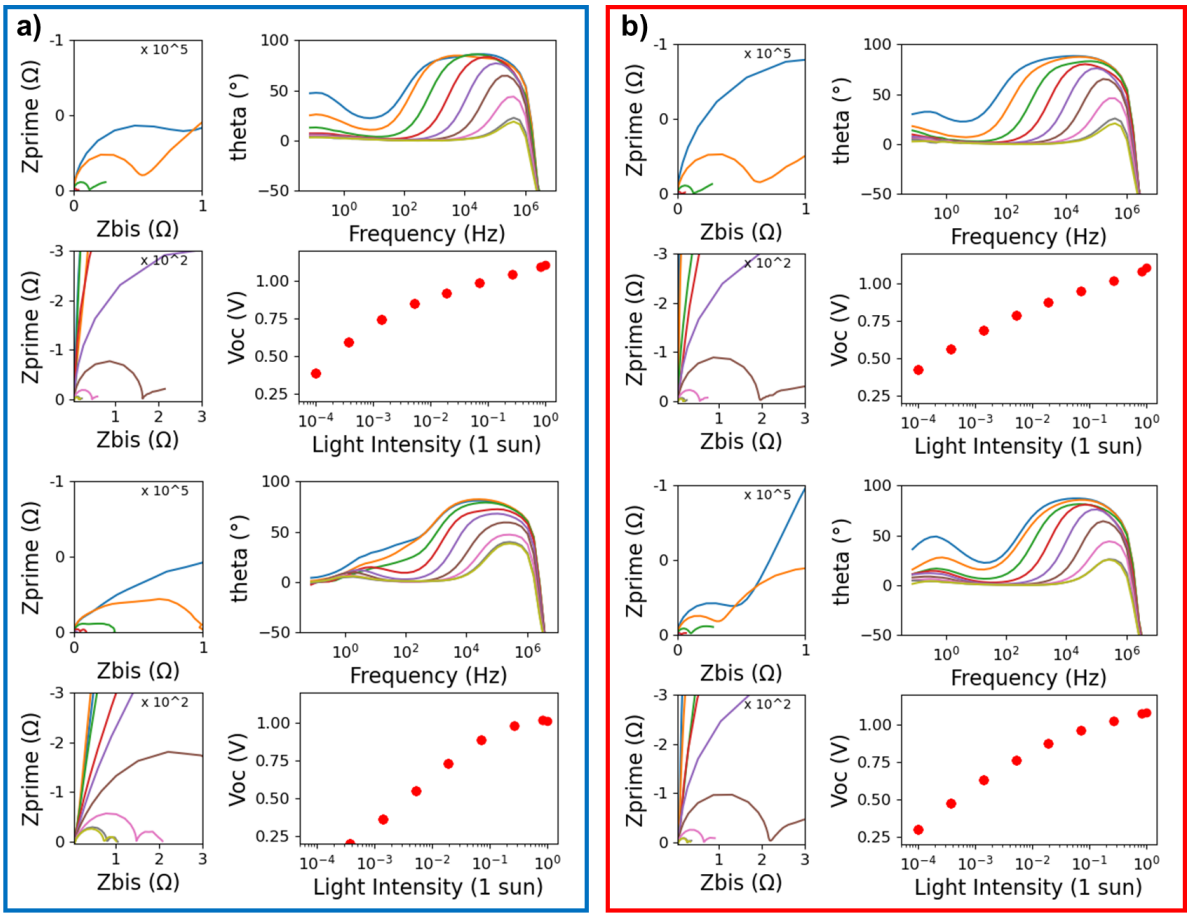

Figure S3. Experimental EIS data for REF (a, blue) and MOD (b, red). PSCs before and after operational stability testing at varying light intensities. EIS of before and after ISOS-L3.

S4. Simulations of EIS features by FLUXIM SETFOS™

To support our hypothesis about the possible causes of the LF shift and the causes for differences between MOD and REF PSC, we used FLUXIM software SETFOS, a program meant to simulate the EIS signal depending on properties of the device stack. Simulated devices were simplified as much as possible inspired by previous work by Anta et al. [6], and the devices were investigated at 0.98 sun and 0.9 V as open circuit voltage. Figure S4 shows simulated phase shift plots from varying cation mobility (Figure S4a) and cation density (Figure S4b) together with the parameters selected as in the table in S4c. After optimizing the impedance curve, the cation (iodide vacancy) mobility was kept still without modifying the standard settings of perovskite solar cell in the program. Modifying the cation density at constant mobility E^{-3} cm^2/Vs did not produce the major changes in EIS ionic signal observed, instead it largely produced changes in the relative magnitude of the high frequency and low frequency signal. It is still possible that the ion density could share minor responsibility for the small increase in LF signal, but the main change (frequency shift) was not observable. On the other hand, when the density of the cation was kept still at $1E^{16}$ cm^{-3}, and the ionic motilities of the cations were modified from E^{-4} to E^2 cm^2/Vs, the simulated signal was greatly influenced in a similar manner to what was observed from experimental EIS before and after operational testing at ~100 mWcm^{-2} and 85 °C (Figure S3), especially regarding the shift of the LF phase peak.

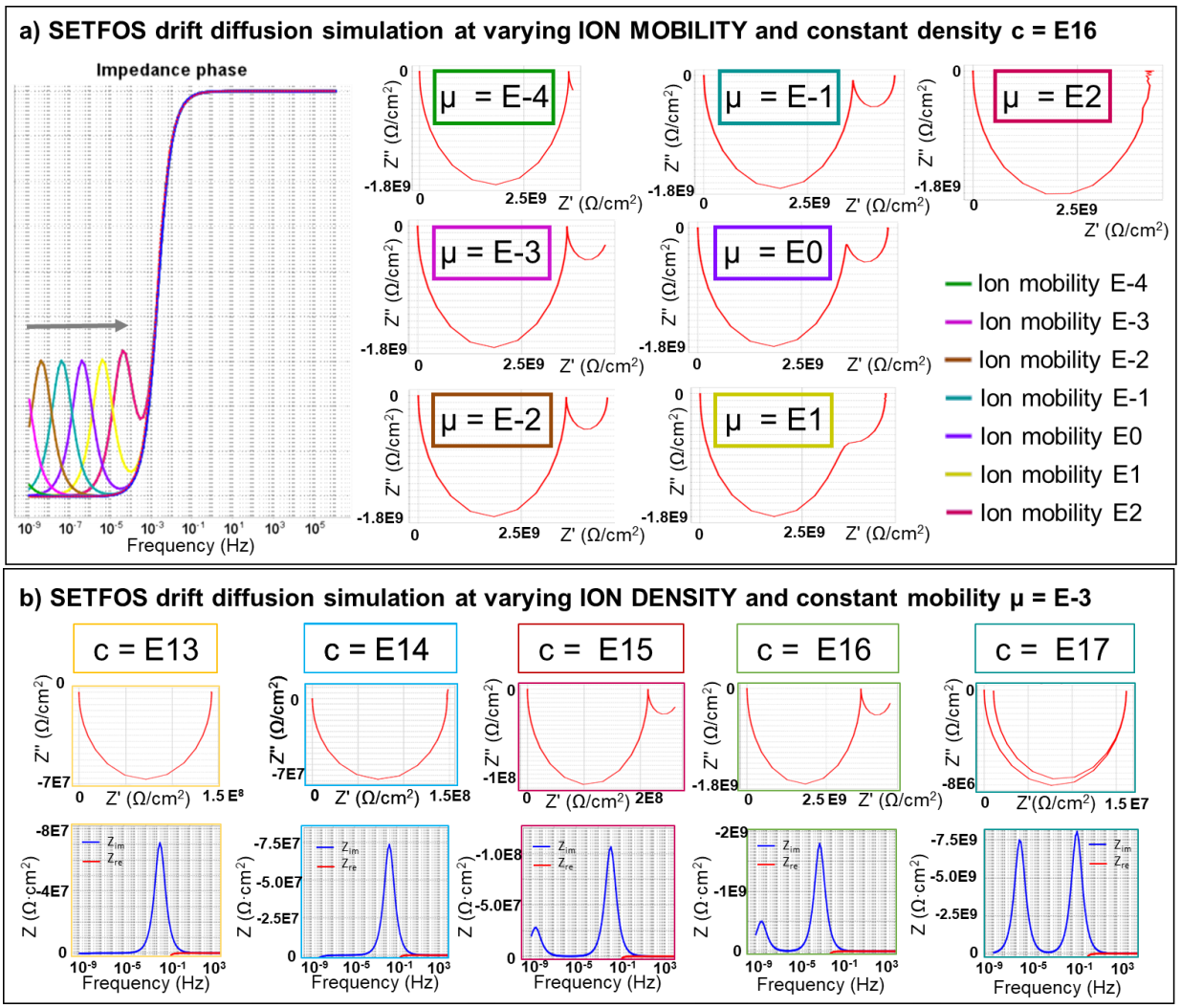

The parameters for drift diffusion were taken from the tables presented by Riquelme et al. [https://doi.org/10.1039/D0NR03058A] with help from J. A. Anta and modified as below:

Electron density: 1E15 cm^{-3}
Electron mobility: 34 cm^2/Vs
Hole density: 1E15 cm^{-3}
Hole mobility:10 cm^2/Vs
Voltage: 0.9 V as open circuit voltage
Illumination intensity: 0.98 sun
Cation (iodine vacancy) concentration (when constant): 1E16 cm^{-3}
Cation (iodine vacancy) mobility (when constant): 1E-3 cm^2/Vs

The spectra was first simulated to looks as similar to what was found in experimental data as possible, then kept constant for variations

Figure S4. SETFOS™ drift diffusion simulations. a) phase shift and EIS spectral simulation when modifying the cation mobility at constant density $1E^{16}$ cm^{-3}. b) EIS Nyquist (top) and Bode plot (bottom) spectral simulation when modifying the cation density at constant mobility $1E^{-3}$ cm^2/Vs. The rest of the parameters for drift diffusion were taken from the tables presented by Riquelme et al.[7]

S5. Additional in-situ XRD

Images of the in-situ X-ray diffraction (XRD) holder under operation is shown with, Figure S5a, and without, Figure S5b, the graphite dome. The selected scan window resulted in continuous scans performed every 45 minutes (Figure S5c). Application of illumination in In-situ XRD was done via controlling the current flowing through a cold white Cree® XLamp® XP-G LED (230-240 mA) using a Keithley SMU that simultaneously measured current and applied voltage bias in connection to the PSC device (Figure S5b) to achieve a similar output current as under the Solar Simulator (JV curves), spectra in Figure S1a. The validity of this method was controlled with spectral measurements, registering intensities slightly above 1 sun (~105 $mWcm^{-2}$, Figure S1a). Application of temperature was done via a ceramic coil in the metal at the sample borders, and the heated part of the stage was separated from the rest of the stage by thermal isolators. The temperature was controlled by a thermocouple and feedback loop through a DC converter.

An example of raw XRD spectral changes at each condition (RT, dark; RT, light; 85 °C, dark; 85 °C, light) is seen in Figure S5d. After fitting a Pseudo Voigt function to each peak in XRD scans, corresponding to the positive interference between crystal planes that give XRD signal, the inter-planar distance *d* was calculated using Bragg's law for each of the perovskite peaks according to

$$n\lambda = 2dsin(\theta) \qquad \text{(Eq. S3)}$$

where *n* is an integer number, λ is the wavelength of the X-rays (1.5418 Å) and θ is extracted from the center position (2θ) of the Pseudo-Voigt fitting. The approximated lattice parameter a_{hkl} for the perovskite peaks with Miller index *h*,*k*,*l*, was calculated according to

$$d = \frac{a}{\sqrt{h^2+k^2+l^2}} \qquad \text{(Eq. S4)}$$

Subsequently Nelson-Riley regression of all a_{hkl} values for each scan determined the accurate lattice parameter *a* at the time of each measurement. A linear regression of a_{hkl} against

$$x = \frac{cos^2(\theta)}{\sin(\theta)} + \frac{cos^2(\theta)}{\theta} \qquad \text{(Eq. S5)}$$

is successfully extrapolated to $x = 0$ for accurate *a* in the case of good cubic coherence of the HP (that gives a linear tendency of a_{hkl} *vs.* x.[8] A selection of Nelson-Riley regressions for the MOD and REF samples presented in Figure 5 are shown in Figure S5e.

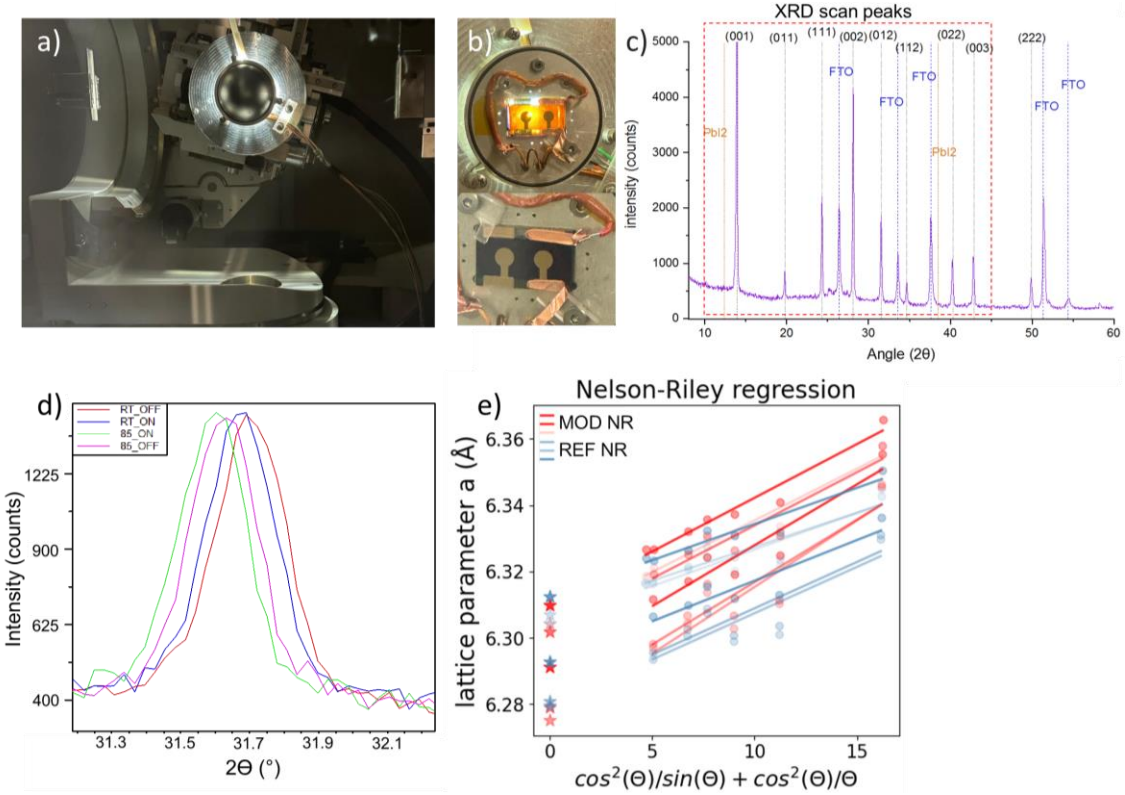

Figure S5. In-situ XRD analysis. a-b) XRD stage during operation X-ray diffraction setup for in-situ experiment with temperature and light in common X-ray diffraction equipment (Malvern-Panalytical) for measurement of thin films, a) Upon measurements the equipment was covered to avoid light interference and the sample was operated only in N_2 gas flow with an X-ray transparent graphite dome b) close up of connected sample without the dome to show the electrical connections (not under real experiment). c) XRD scan selection included perovskite peaks (001), (011), (111), (002), (012), (112), (022), (003) with 2θ ≈ 13.9°, 19.8°, 24.4°, 28.2°, 31.6°, 40.4°, 42.9°, substrate peaks FTO (100), (110), (111) with FTO (110) at 2θ ≈ 24.6° used for alignment control, and defect peaks at 2θ ≈ 12.6° PbI_2 and 2θ ≈ 34.7°. d) XRD peak progression example for the 4 discrete conditions applied. e) Nelson-Riley regression analysis.

Curiously, application of each stress-condition (dark+RT, light+RT, dark+85 °C, light+85 °C) generated XRD patterns corresponding to a specific lattice parameter for both REF and MOD dependent on the stress-condition, without changes over time under static conditions, as seen in Figure 6b.

The static lattice distances depending on the conditions were reproduced in several experiments beyond what is reported in the main article, including cycling experiments. Figure S6 visualizes the results for REF and MOD of repeatedly applying and removing the operational conditions of 85 °C and ~105 mWcm^{-2}, demonstrating the discrete and consistent response of joined light and temperature provoked expansion in both REF and MOD.

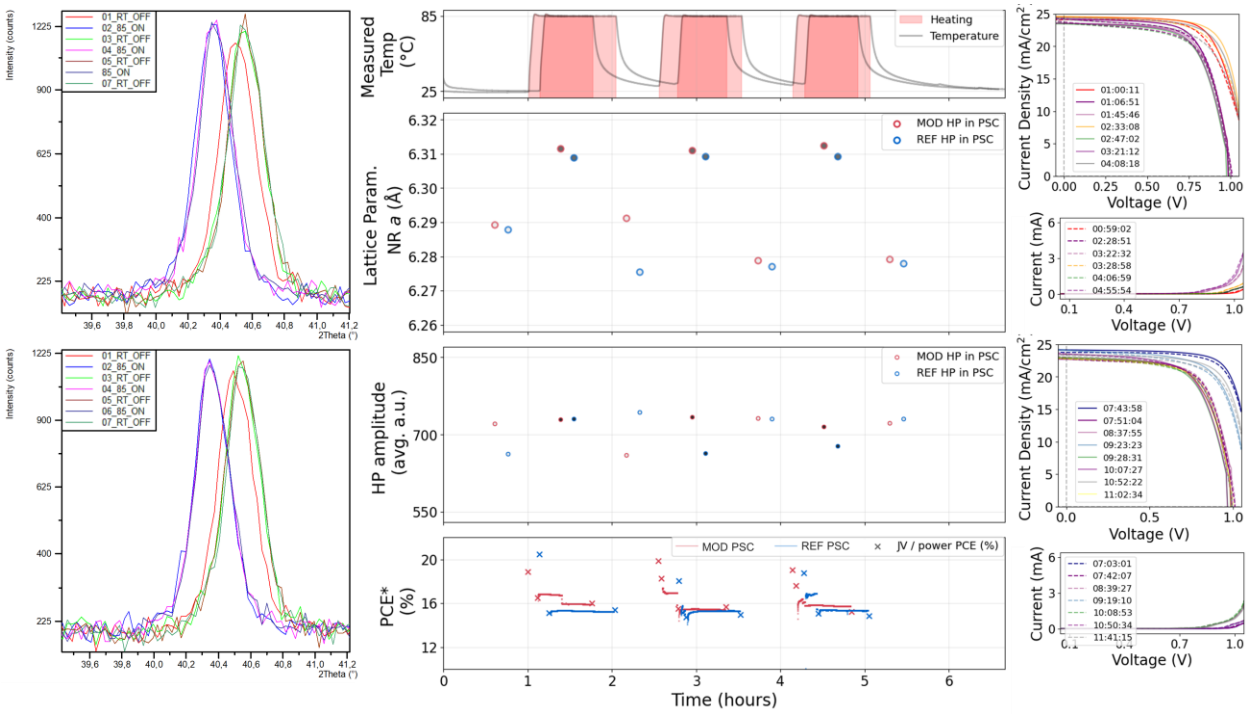

Figure S6. ON and OFF cycling operational test in-situ XRD shows the discrete lattice changes and performance changes when repeatedly applying and removing the operational conditions of 85 °C and ~105 mWcm^{-2}.

To further relate the structural changes of the perovskite to each stressor, light and heat were applied sequentially. By applying light and temperature sequentially and by cycling the light on and off we could decouple effects produced during heating from illumination or heating from the stage. In the experiment presented in Figure 5, after heating to 85 °C, the illumination was turned off and on twice. Furthermore, an additional left shift in XRD peaks occurred when turning the light on at 85 °C, in agreement with previous reports stating that illumination may produce additional internal heating of a perovskite film. [9-12] At such high operating temperatures as 85 °C, the light induced heat does not reach the thermocouple in the sample stage, nevertheless, if can be registered by XRD. We cannot rule out that an additional expansion from light or generated carriers might also occur.[2, 13]

After the longer stress at 85 °C, the effect of switching the light on and off was again monitored during and after cooling down, Figure 5a section (4). From the data obtained at stage 2 and stage 5 we can estimate the perovskite thermal expansion coefficient (from conductive heating). During recovery at RT, the holder temperature was set to the measured increase in temperature when the LED was switched on, to contrast the irradiance heating and confirm the existence of two different heat-sources, Figure 5 section (5). When turning on the illumination at room temperature (A) the temperature increased from 26.5 °C to 30.1 °C and we observe a lattice parameter increase of ~ 0.006 to 0.008 Å. When the temperature holder is set to 30.1 °C we observe a smaller lattice parameter increase below 0.003 Å (B).

Table S1.

	ΔT (K)	Δ*a* (Å)	CTE_P (Δ*a* / ΔT)
A (L+85 °C)	85-27 = 58	0.02 / 6.29 ≈ 0.00318	$0.00318/58 \approx 5.48 \cdot 10^{-5}$ /K
B (L)	30.1-26.5 = 3.60	0.006 / 6.28 ≈ 0.00127	$0.00127/3.60 \approx 3.596 \cdot 10^{-4}$ /K
C (30.1 °C)	3.6	0.002 / 6.28 ≈ 0.000318	$0.000318/3.60 \approx 8.846 \cdot 10^{-5}$ /K

Which indicated poor heat conduction from the perovskite layer to the stage, and/or other causes for expansion.

Figure S7a shows how no new crystalline features appeared under prolonged stress, including changes in PbI_2 content. No deviation from cubic structure was detected in any of the conditions, including no major changes in microstructure (Figure S7b-c).

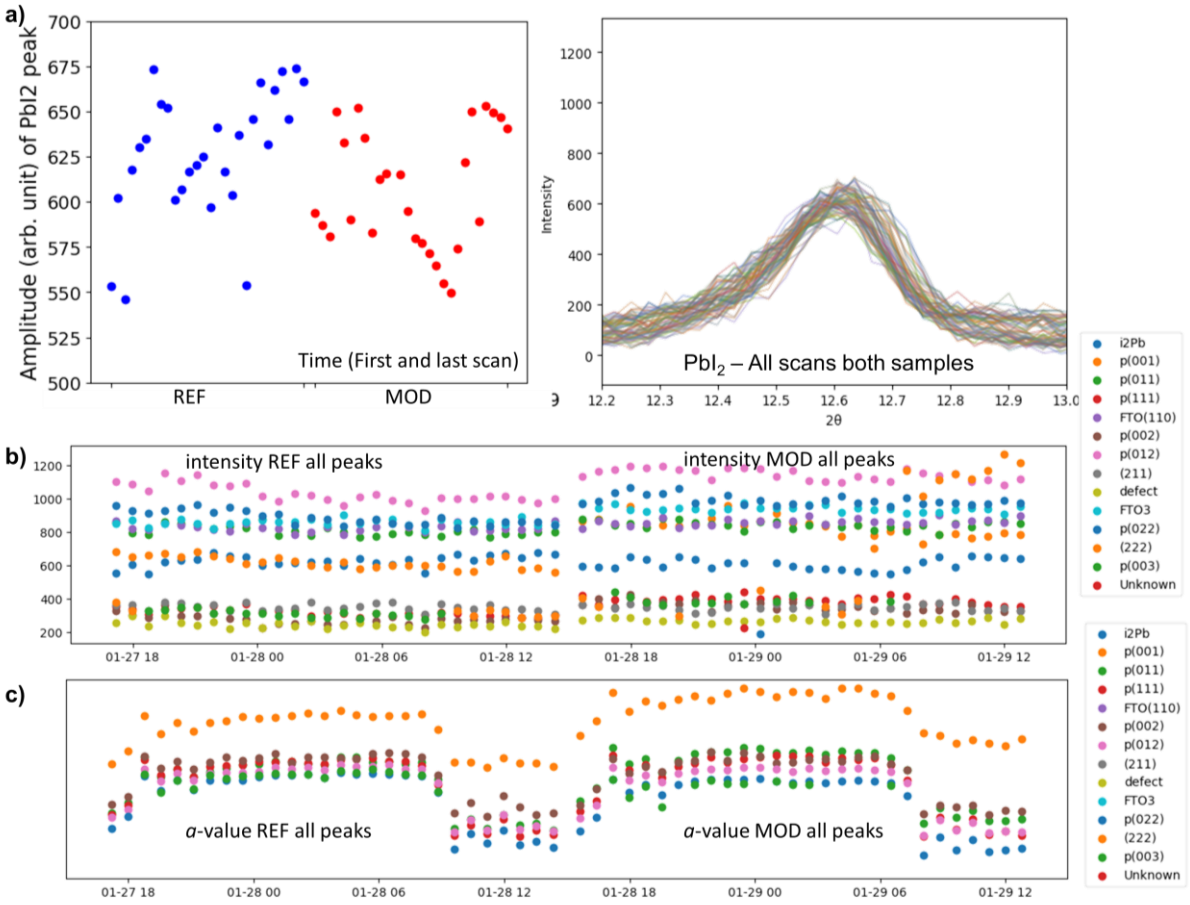

Figure S7. a) PbI_2 content over time unchanging. b) intensity of all XRD peaks over time for the two samples testes subsequently (the two samples from main Figure 5) c) lattice parameter a.

S8. Additional Electron Microscopy

One PSC of each variation (MOD and REF) was split down the middle, and one half was treated at ~100 $mWcm^{-2}$ and 85 °C in the XRD holder (at high N_2 flow) for 20 hours, while the other half was kept in N_2 flow during the time.

Cross-section scanning electron microscopy (CS-SEM) was performed immediately after stress on the exposed surface. Figure S8a and S8b show cross-section Scanning Electron Microscope (CS-SEM) images of

MOD and REF solar cell halves performed ~30 minutes after removal from the stress conditions. Sharp, dark grain boundaries with void formations are seen after treating MOD for 20 h at ~>1 sun and 85 °C, while REF devices show bright, seemingly wider boundaries that appear to extend into the spiro HTL layer (Figure S8a), not present in the other (untreated) half of the divided device (Figure S8b). This is in accordance with bright lines reported previously in in-situ TEM during degradation of PSC under elevated temperature (50-60 °C) and illumination.[14] The samples were measured shortly after treatment, and reduction in width of the brighter grain boundaries in REF over time and related voids during measurements indicated that the formation of these grain boundary regions are somewhat reversible, and with large beam sensitivity. It was clear that the largest differences between degraded REF and MOD were found at grain boundaries and at the HP/HTL interface, while the untreated halves looked alike. The void formation in treated MOD seen in CS-SEM is concerning, and can be related to small metallic lead and PbI_2 seen in TEM (Figure S11 and S12), indicating that there is room for future improvement in the modification strategy.

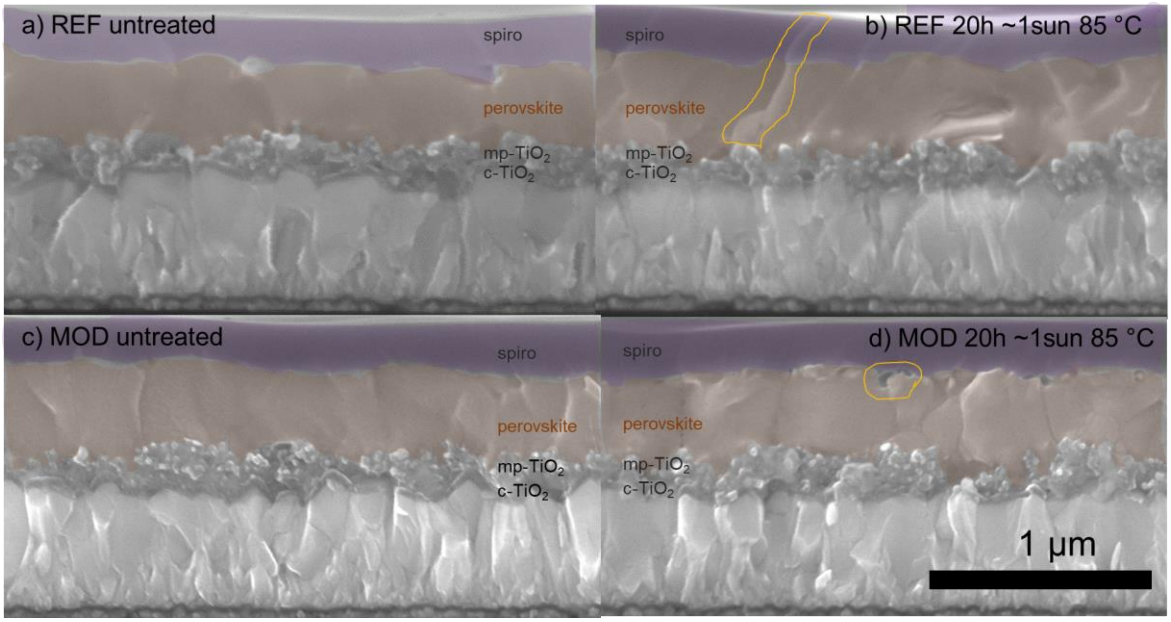

Figure S8. a). Cross-section SEM images with shading and labels to mark the perovskite layer and its interfacing selective transport materials. Samples of ~16% PCE split in half, one part untreated after storage in nitrogen since fabrication and one part treated at ~1 sun LED illumination and 85 °C in the XRD holder for 20 h. a-b) REF n-i-p PSC, c-d) MOD PSC with HP:H3PP and MXene:H3PP additives.

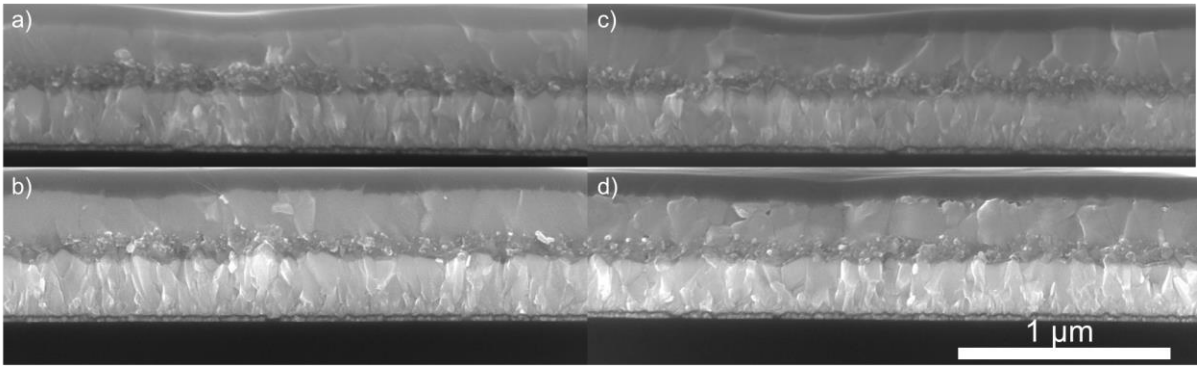

Figure S8 b). SEM Cross-section at lower magnification. a) REF untreated b) MOD untreated c) REF treated d) MOD treated.

Later, HRTEM was used to take a closer look on HP samples scratched from the HP/spiro-OMeTAD surface of the device-halves. Figure S9 shows HP sections HRTEM and EDX from untreated REF and MOD PSC halves. At some flake boundaries of MOD, a small phosphate signal can also be detected, confirming that

the H3PP additive is present. In non-treated MOD there was no Ti signal inside HP grains, but plenty just outside of them. There is also a very small phosphor signal. Grains seems to go all the way to the edge of sections.

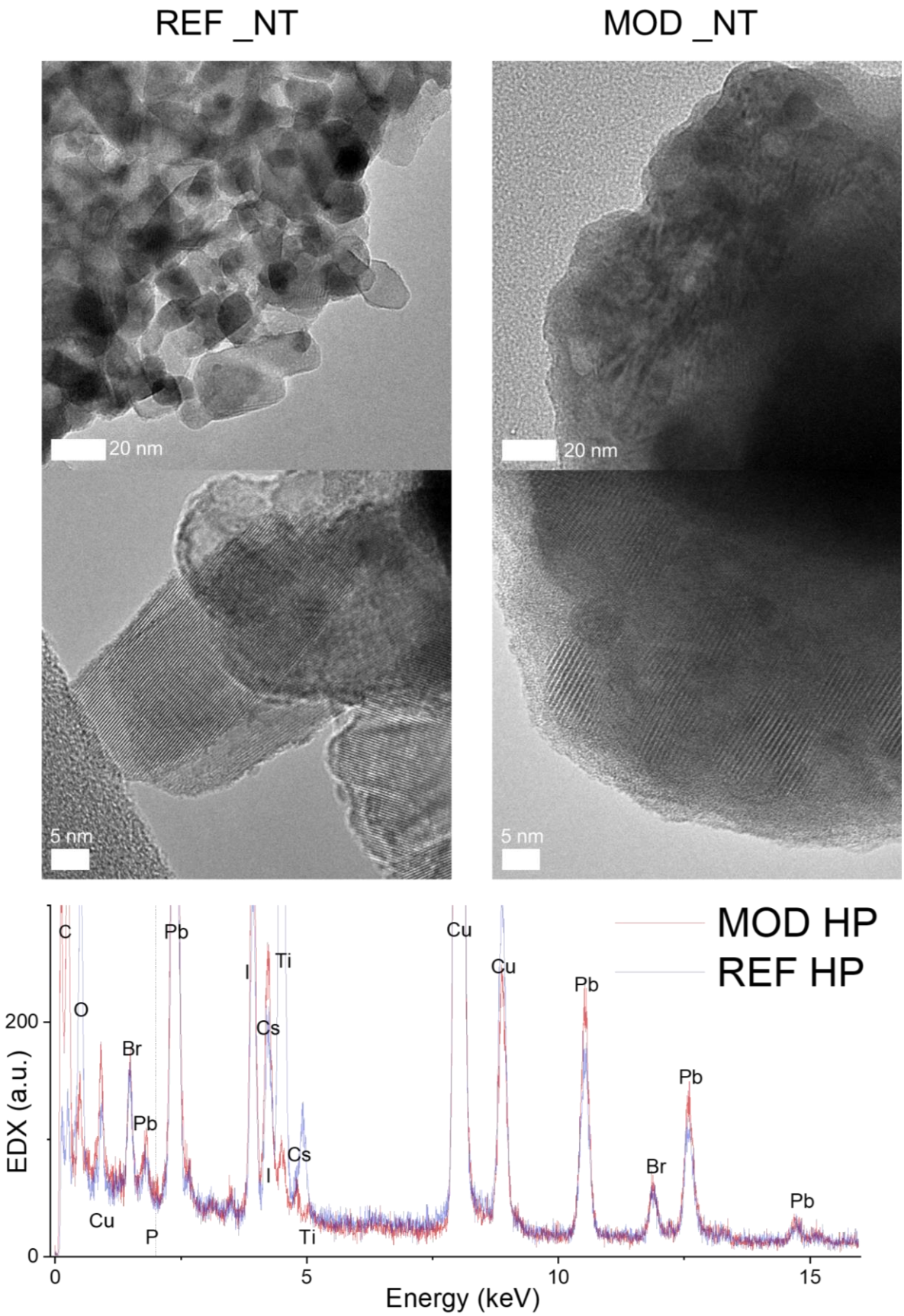

Figure S9. Non-treated REF and MOD HP with EDX signals.

Figure S10 show colored HRTEM images to quantify the amorphous section produced in REF and MOD respectively.

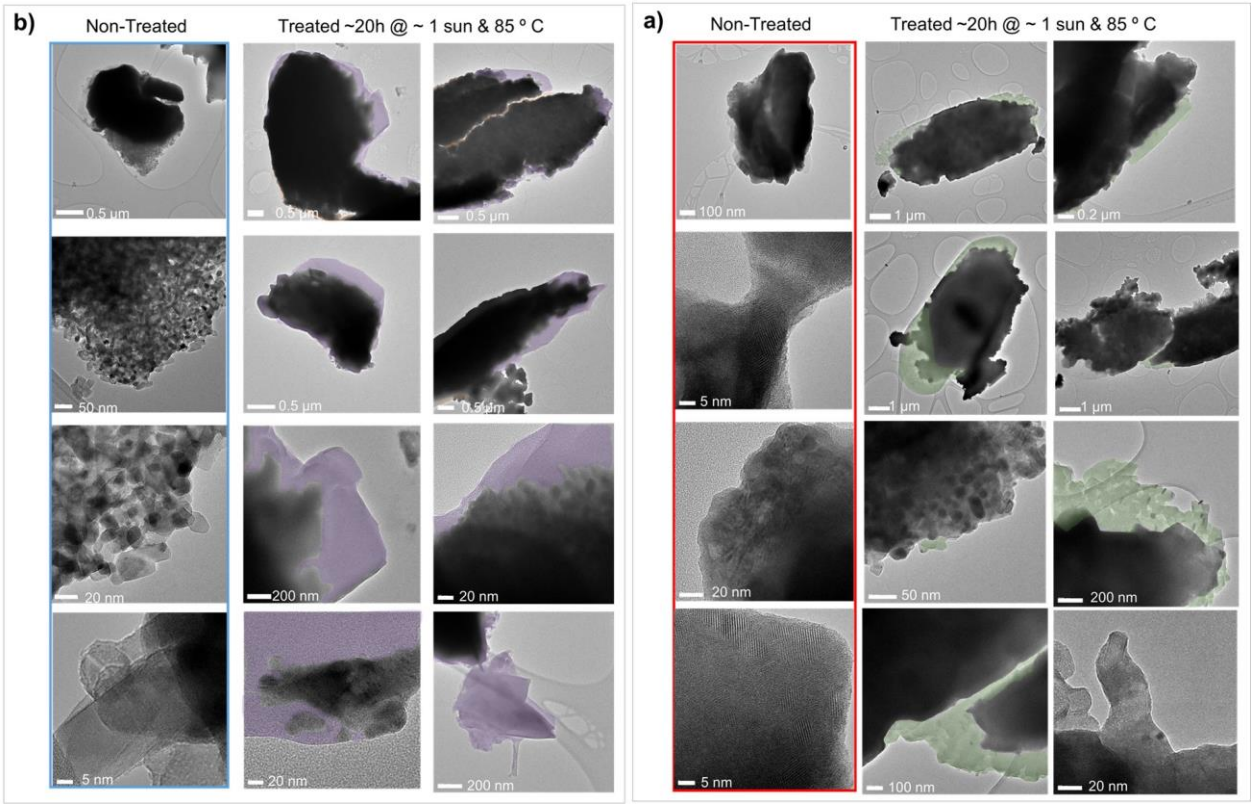

Figure S10. TEM images of different grains showing the prevalence of amorphous phase in REF and MOD.

A closer look at the amorphous phase formed in MOD and REF is shown in Figure S11, where we observe large differences in the phase constitution of the phase in the two cases. In HP taken from the treated REF HP, the amorphous phase surrounds the grain, and a closer look by EDX reveals that the amorphous phase has a high carbon content. In HP from treated MOD on the other hand, there is almost no amorphous phase, and the one found looks like a solid emulsion of many dark particles. A closer look with STEM (where now denser particles are brighter), reveals that there are even more particles than expected in any new phase formed in the MOD sample, and EDX in STEM configuration (with higher resolution) of the bright particles shows predominantly signals that that can be related to TiO_2, MXene or HP composition, but also a high carbon signal.

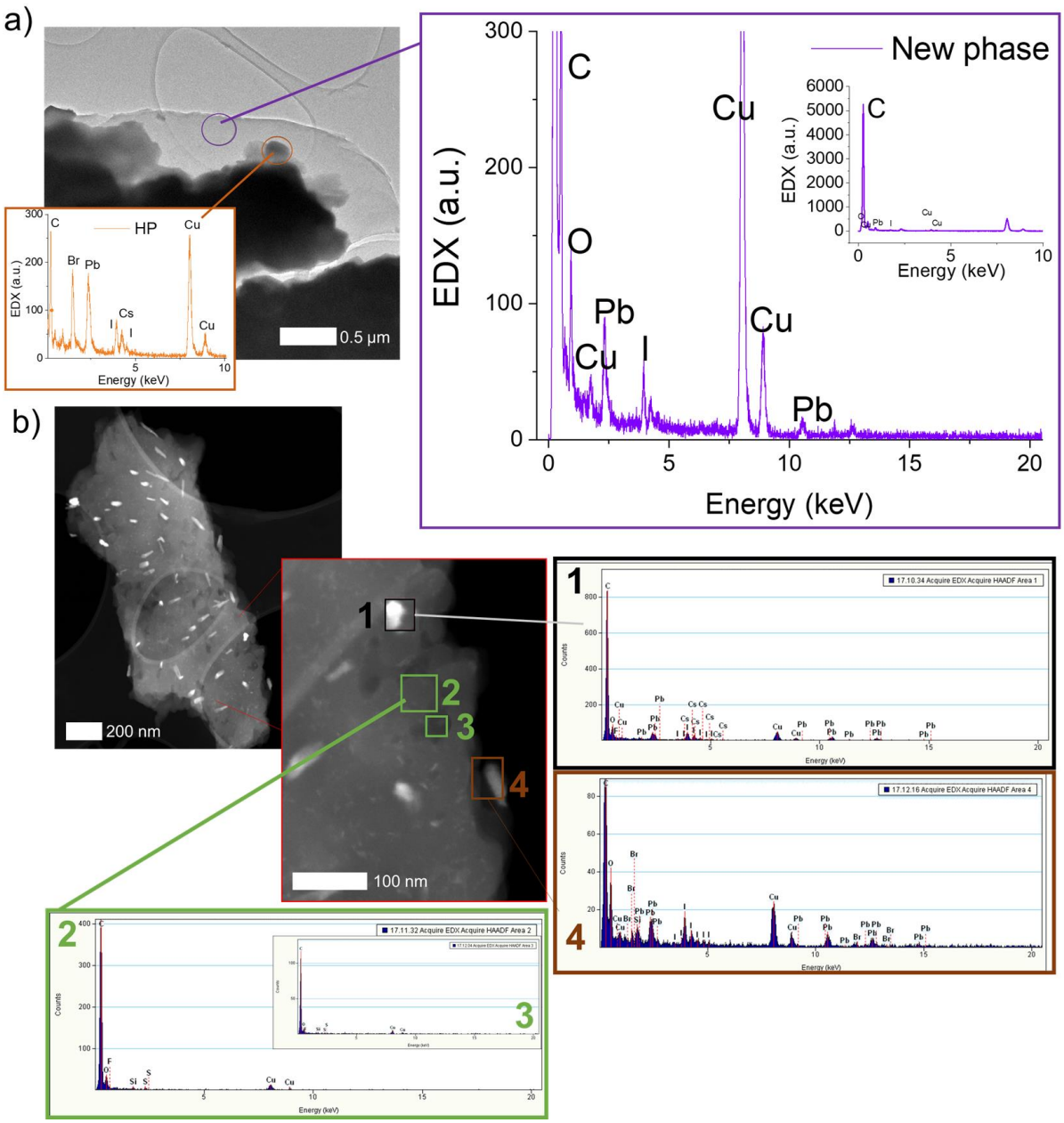

Figure S11. EDX studies of amorphous parts surrounding HP flakes from treated a) REF, b) MOD. After ~105 mWcm^{-2} and *85* °C *for ~20 h followed by ~ 1-week rest in* N_2.

The EDX studies revealed that MOD HP seemed more likely to form metallic lead in the case of degradation, rather than forming the amorphous material from surface decomposition. Large lead containing particles of ~20 nm diameter could be detected in treated MOD (Figure S12). In comparison, small titanium and oxygen containing clusters showed particles of below 4 nm size.

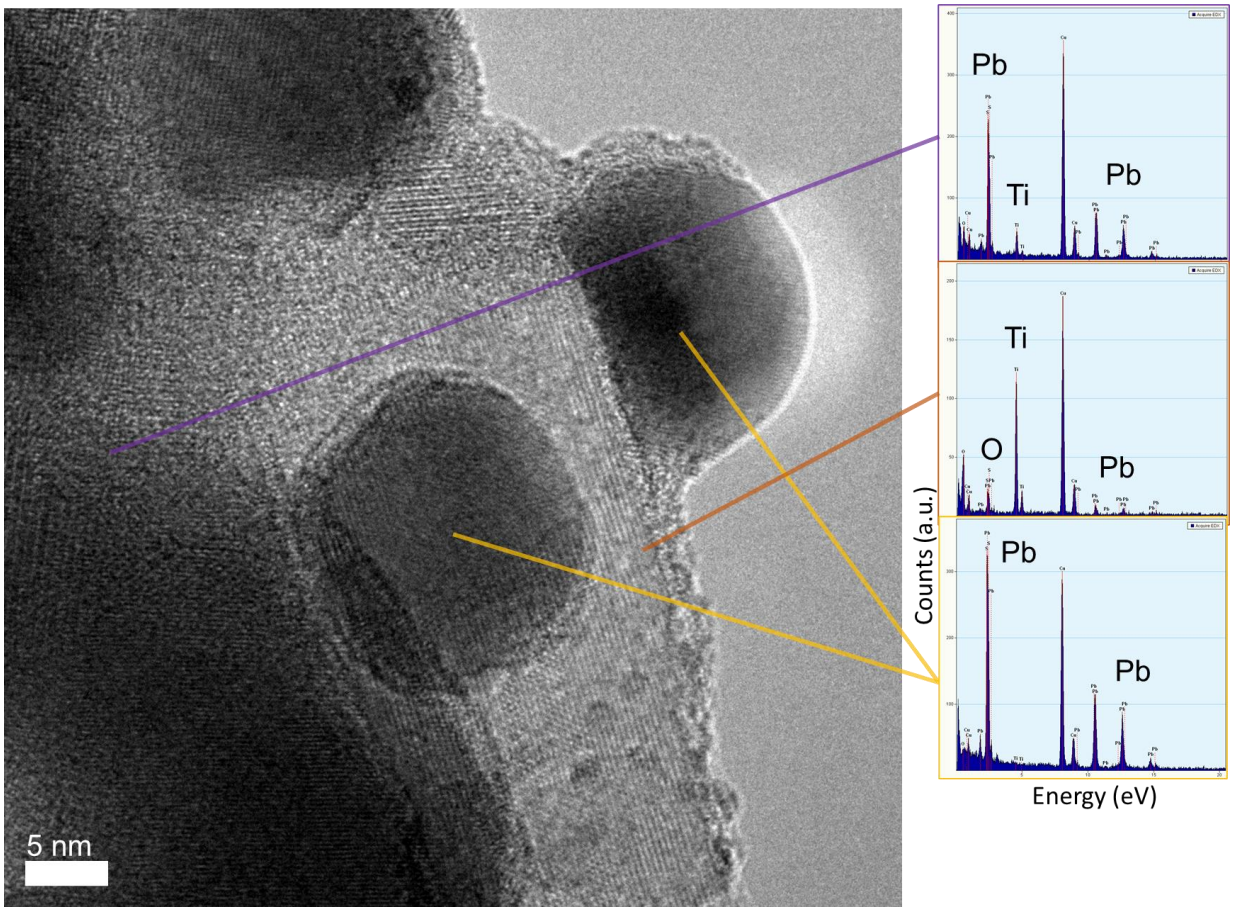

Figure S12. Identified defects in a HP sample from the treated MOD PSC characterized by HRTEM and EDX.

References

1. Karimipour, M.; Paingott Parambil, A.; Tabah Tanko, K.; Zhang, T.; Gao, F.; Lira-Cantu, M., Functionalized MXene/Halide Perovskite Heterojunctions for Perovskite Solar Cells Stable Under Real Outdoor Conditions. *Advanced Energy Materials* **2023,** *13* (44), 2301959.
2. Baumann, F.; Karimipour, M.; Padilla-Pantoja, J.; Chávez-Angel, E.; Caicedo Roque, J. M.; Pouteaux, R.; Alcalá Ibarra, A.; R. Raga, S.; Santiso, J.; Lira-Cantu, M., Strain in Halide Perovskites and Solar Cell Stability: Accelerated Stress Tests under Bias Voltage. *ACS Energy Letters* **2025,** *10* (1), 476-483.
3. Bou, A.; Pockett, A.; Raptis, D.; Watson, T.; Carnie, M. J.; Bisquert, J., Beyond Impedance Spectroscopy of Perovskite Solar Cells: Insights from the Spectral Correlation of the Electrooptical Frequency Techniques. *The journal of physical chemistry letters* **2020,** *11* (20), 8654-8659.
4. Ebadi, F.; Aryanpour, M.; Mohammadpour, R.; Taghavinia, N., Coupled Ionic-Electronic Equivalent Circuit to Describe Asymmetric Rise and Decay of Photovoltage Profile in Perovskite Solar Cells. *Scientific Reports* **2019,** *9* (1), 11962.
5. Contreras-Bernal, L.; Ramos-Terrón, S.; Riquelme, A.; Boix, P. P.; Idígoras, J.; Mora-Seró, I.; Anta, J. A., Impedance analysis of perovskite solar cells: a case study. *Journal of Materials Chemistry A* **2019,** *7* (19), 12191-12200.

6. Almora, O.; Cho, K. T.; Aghazada, S.; Zimmermann, I.; Matt, G. J.; Brabec, C. J.; Nazeeruddin, M. K.; Garcia-Belmonte, G., Discerning recombination mechanisms and ideality factors through impedance analysis of high-efficiency perovskite solar cells. *Nano Energy* **2018,** *48*, 63-72.
7. Riquelme, A.; Bennett, L. J.; Courtier, N. E.; Wolf, M. J.; Contreras-Bernal, L.; Walker, A. B.; Richardson, G.; Anta, J. A., Identification of recombination losses and charge collection efficiency in a perovskite solar cell by comparing impedance response to a drift-diffusion model. *Nanoscale* **2020,** *12* (33), 17385-17398.
8. Harrington, G. F.; Santiso, J., Back-to-Basics tutorial: X-ray diffraction of thin films. *Journal of Electroceramics* **2021,** *47* (4), 141-163.
9. Varjopuro, J.; Kamppinen, A.; Poskela, A.; Karhu, J. A.; Lindfors, A. V.; Miettunen, K., Computational simulation of perovskite and silicon solar panel operating temperatures in varying ambient conditions. *Solar Energy Materials and Solar Cells* **2025,** *290*, 113657.
10. Peterson, K. A.; Patterson, A.; Vega-Flick, A.; Liao, B.; Chabinyc, M. L., Doping molecular organic semiconductors by diffusion from the vapor phase. *Materials Chemistry Frontiers* **2020,** *4* (12), 3632-3639.
11. Haeger, T.; Heiderhoff, R.; Riedl, T., Thermal properties of metal-halide perovskites. *Journal of Materials Chemistry C* **2020,** *8* (41), 14289-14311.
12. Baumann, F.; Raga, S. R.; Lira-Cantú, M., Monitoring the stability and degradation mechanisms of perovskite solar cells by in situ and operando characterization. *APL Energy* **2023,** *1* (1).
13. Kim, D.; Yun, J. S.; Sharma, P.; Lee, D. S.; Kim, J.; Soufiani, A. M.; Huang, S.; Green, M. A.; Ho-Baillie, A. W. Y.; Seidel, J., Light- and bias-induced structural variations in metal halide perovskites. *Nature Communications* **2019,** *10* (1), 444.
14. Yang, B.; Dyck, O.; Ming, W.; Du, M.-H.; Das, S.; Rouleau, C. M.; Duscher, G.; Geohegan, D. B.; Xiao, K., Observation of Nanoscale Morphological and Structural Degradation in Perovskite Solar Cells by in Situ TEM. *ACS Applied Materials & Interfaces* **2016,** *8* (47), 32333-32340.